Quantitatively Assessing the Presence and Effect of Bars on Stellar Dynamics and Galaxy Formation

By
Thomas Mills
210055795

School of Mathematics, Statistics and Physics
Newcastle University

May 2025

Abstract

This project is a computational study into quantitatively assessing the presence of bars in galaxies and investigating their impact on stellar dynamics and galaxy evolution. Galaxy models composed of Sérsic light profiles were fitted using a non-linear search algorithm to James Webb Space Telescope (JWST) images and model comparisons were performed between barred and unbarred configurations. The barred models included an additional low-index (n=0.5) Sérsic component to represent a bar. It was shown that by comparing fit quality – via log likelihood values ($\mathcal{L}$) – it was possible to determine whether a galaxy is more likely to host a bar. From this, $\Delta\mathcal{L}$ thresholds were determined, to provide consistent quantitative bar indicators. It was observed that intensity (I) dropped around the bar within the corotation disk, supporting contemporary research showing that bars reduce specific star formation (STF) within the co-rotation disk. Further visual analysis uncovered that bars also act as stellar nurseries, ultimately accelerating nuclear star formation. The entire length of the bars were observed to possess a higher intensity in comparison with the rest of the galaxy, climaxing towards the centre. Supporting cutting-edge research on bars' role in stellar dynamics and galaxy formation.

1 Introduction

Galaxy catalogues are essential for astronomy [1], compiling positions, brightness, and morphology. Identifying bars—one of the most significant contributors to galaxy evolution[2]—fills a major catalogue need. Catalogues enable statistical analysis of galaxy populations, structural evolution and environmental effects by providing standardised datasets for comparing observations across different surveys and wavelengths. With advancements, like JWST, catalogues are becoming more detailed, offering deeper insights into galaxy formation and dynamics.

Galaxies can take different forms, such as ellipticals, with smooth stellar distribution or disks with a common spiral pattern. Bars are common within disk galaxies. When considering prominent and weak bars, a bar fraction is usually found to be ~ 2/3 [3]. The central bar forms as a way of creating stability, by redistributing angular momentum within the galaxy. The bar formed subsequently acts as a conduit for material, redistributing gas and dust, thus driving internal evolution [4]. Bar length and strength also indicate galaxy age – stronger, longer bars mark older systems [5], allowing them to act as a powerful dating tool.
This study will focus on confirming a quantitative method for determining the presence of a bar within a galaxy. For face-on galaxies it is possible to be visually confident about the presence of a bar, their unique structure, size and colour ensure this. This is harder for side-on galaxies but still possible as barred galaxies often display 'peanut' or 'X' shaped bulges from the side [6], due to vertical instability caused by the bar, meaning that the bar essentially 'flops' up and down from the centre [4]. So why the need of quantitative assessment? Quantitative methods avoid subjective bias/human error that comes from purely visual inspection, bar strength can't reliably be judged by eye and due to the large number of galaxies observed it is inefficient to have an analysis process done by the human eye alone.

Figure 1: Barred spiral galaxy NGC 1300. Taken from [7].

Previous work has addressed this challenge through automated and quantitative bar detection techniques. For instance, Nightingale et al. [8] developed "PyAutoGalaxy", a tool that uses multiwavelength modelling and light profile fitting to identify and characterize bars. By applying parametric models like the Sérsic and exponential profiles, they could isolate bar features and assess their prominence objectively [8]. Their method proved reliable for complex galaxies and scaled well with large datasets. This aligns closely with the goals of this study and has informed the approach to confirming bar presence quantitatively, contributing to more efficient and consistent galaxy classification.

The most up to date contemporary research is showing that strong-barred galaxies display the lowest specific star formation rate (SFR/M_*) and unbarred galaxies displaying the highest specific SFR (figure 2). A reason for reduced SFR in barred galaxies is due to bars quenching star formation. Bar induced shocks and shear can stabilise gas against collapse by increasing turbulence and thus inhibit star formation. This is possible since the bar collects most of the gas inside the co-rotation radius (defined by (1.1)) during the formation phase [9][10][11]. Another reason for reduced SFR in barred galaxies is because of bar-induced torque, which drives gas flows into the centre of the galaxy. Enhancing nuclear star formation and making the region close to the bar devoid of fuel for further star formation [9][10][11].

$$\mathrm{V_{circ}}(R_{cr}) = \Omega_{bar} \tag{1.1}$$

Where, $\mathrm{V_{circ}}$ is the angular velocity of the disc, Ω_{bar} is the bar pattern speed and $\mathrm{R_{cr}}$ is the co-rotation radius [12].

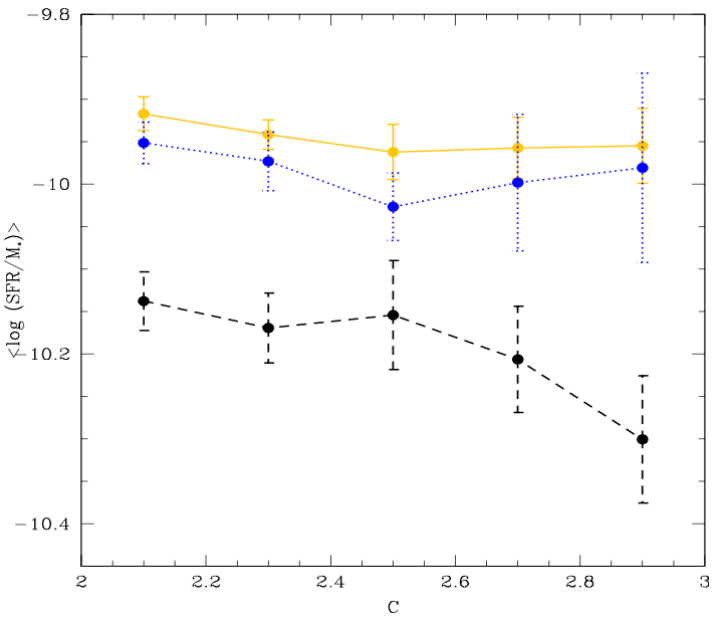

Figure 2: Specific star formation rate (log(SFR/M∗) as a function of concentration index (C) for unbarred (Yellow), weak-barred (blue) and string barred (black) galaxies. Taken from [2].

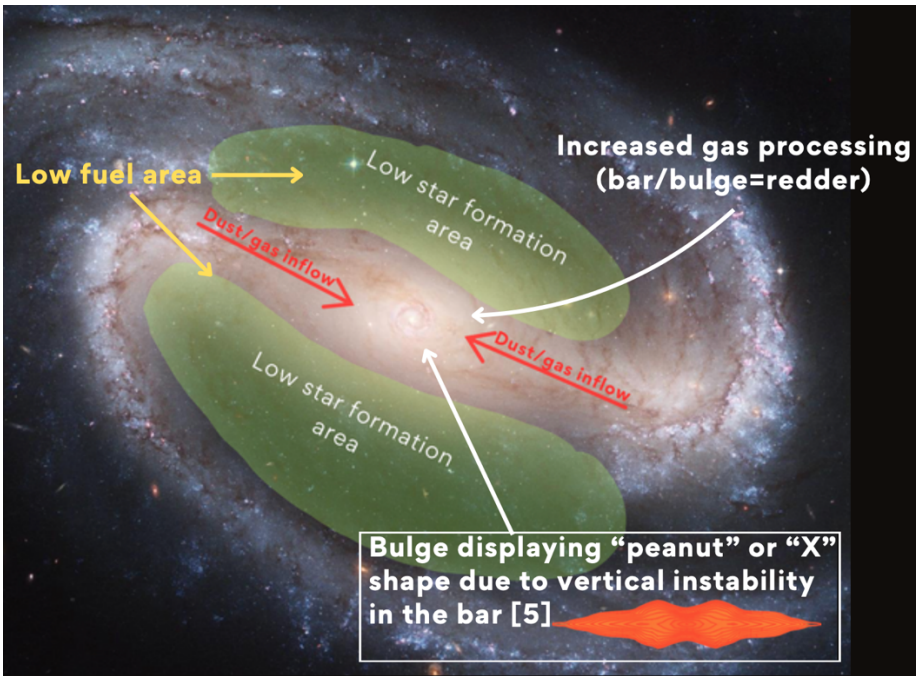

Figure 3: Schematic of barred galaxy. Adapted from [7].

Other state of the art research is also finding that bars do more than shape galaxies – they actively drive internal evolution. Research shows that bars act as stellar nurseries by funnelling gas inward from outer regions, concentrating material in the central areas and along the bar itself [2][13][14]. This inflow gas provides the fuel necessary for enhanced star formation. Understanding how star formation is distributed along the bar can therefore offer insights into the evolutionary state and growth patterns of disk galaxies [13].

This study investigates SFR within the co-rotation disk and the dynamical influence of bars on secular galaxy evolution, by analysing intensity profiles and structural morphology once the presence of a bar has been confirmed. By relating intensity, I to stellar activity ($I \propto stellar\ activity$) it was then possible to draw conclusions about the effect of bars and review the contemporary literature.

2 Method and Theoretical Background

In this section, we describe the how the accuracy of the modelling and model comparison were tested to ensure accurate results, as well as a description of the fitting method and how JWST image analysis was carried out.
To support the modelling/fitting process, a tutorial handbook containing example coding methods and fitting strategies was provided [15], from which the method code was built.

Overview of project:

1. Create barred (double Sersic) and unbarred (single Sérsic) galaxy models.
2. Fit barred-model to simulated barred-images (bar_0/bar_1) to verify the accuracy of the light profile fitting analysis.
3. Fit models to bar_0/bar_1 and do model comparison to verify the barred model produces a better fit.
4. Fit models to simulated unbarred-image (no_bar) to verify the barred model fit does not improve for unbarred images.
5. Fit models to JWST images and conduct model comparison to determine the presence of a bar.

2.1 Modelling

For the project, a galaxy model was created with a Sérsic light profile. A Sérsic profile was used as it is a common choice amongst astronomers, able to effectively model both spiral and elliptical galaxies [16]. Sérsic profiles are defined by:

$$I_{Ser}(\eta_1) = Iexp\left\{-k\left[\left(\frac{\eta}{R}\right)^{\frac{1}{n}} - 1\right]\right\} \tag{2.1.1}$$

Where η are elliptical coordinates (arc-seconds), defined by (2.1.2). I is intensity normalisation (electrons per second). R is effective radius (arc-seconds). n is Sérsic index. k=2n-1/3 (const) [17].

$$\eta = (\epsilon_1, \epsilon_2) \tag{2.1.2}$$

Where,

$$\epsilon_1 = \frac{1-q}{1+q}\sin(2\phi) \tag{2.1.3}$$

$$\epsilon_2 = \frac{1-q}{1+q}\cos(2\phi) \tag{2.1.4}$$

are the elliptical components. q is axis-ratio of the ellipse and ϕ is angle (degrees) used to rotate the grid.

The Sérsic index is a free parameter that modulates the shape of the Sérsic profile [18]. A Sérsic index n=1 results in an exponential profile, while n=4 is equivalent to the de Vaucouleurs profile [19]. The Sérsic index determines how concentrated the light is towards the centre, with higher n indicating a more concentrated profile [20] (see Graham & Driver [20], for a complete reference to the related mathematical expressions). Bars would fall on the lowest end of the Sérsic index ~ 0.5, due to their elongated profile. For the unbarred galaxy, one disk component would satisfy but to identify a bar within a galaxy an additional light profile was included in the model to act as a bar [21]. The bar component had its Sérsic index forced to n=0.5 by confining its priors with a lower limit of 0.5 and an upper limit of 0.51. Sérsic index priors have a lower limit of 0.5, lower values are unphysical [22].

The grids through the project were defined in units of arc-seconds (“). The pixel scale parameter in the code set how many arc-seconds each pixel represents. This was adapted to fit the simulated images, with a pixel scale of 0.06. The same as the JWST images [23]. Visual inspections of ‘bar_0’ and ‘bar_1’, were carried out to determine the masking radius. Masking out regions with low signal-to-noise ratios is essential for concentrating on regions where the galaxy is clearly detected, leading to more accurate fitting results.

PyAutoGalaxy was used for its ability to fit complex galaxy morphologies and scale to large datasets [8]. The ‘LightProfile’ and ‘Galaxy’ objects created light profiles and grouped profiles at a set redshift for efficient modelling [8]. The ‘autogalaxy.AnalysisImaging’ function contained the $\mathcal{L}$ function that the non-linear search calls to fit the model to the data [8].

2.2 Fitting

The barred galaxy model was fitted to ‘bar_0’ and ‘bar_1’, with expected effective radii (R_E) of 0.3 and 0.8 effectively. By producing maximum log likelihood results that match R_E, it confirms the accuracy of the light profile fitting analysis. The non-linear search optimization, Nautilus nested search sampling algorithm was used to find the parameter values that best describe the data.

The log likelihood calculations, underpinned by (2.2.1) [15][24], were integral to the project, so it was important for them to be accurate.

$$\mathcal{L} = -\frac{1}{2}(\chi^2 + \sum_{i=1}^{I} \ln[2\pi\sigma_i^2]) \tag{2.2.1}$$

Where $\mathcal{L}$ is log likelihood, χ^2 is chi-squared, defined below [15][24]. The second term is the noise normalisation and remains fixed as the noise map is constant during fitting. The noise map gives you the variance, σ^2 of noise at each data point. The higher the $\mathcal{L}$ the better the fit.

$$\chi^2 = \sum \frac{(O_i - E_i)^2}{E_i} = \sum \left(\frac{model_data}{noise_map}\right)^2 \tag{2.2.2}$$

Where O_i is the observed value, E_i is the expected value. *model_data/noise_map* is the χ^2-map. The χ^2-map is squared to ensure all values are positive. Without this the +/- residuals

would cancel each other out, leading to inaccurate assessment of the models fit to the data. Lower the χ^2, the fewer residuals exist between the model fit and data, indicating a better overall fit.

Initially, the code didn't produce the correct R_E for either simulation to verify accurate fitting analysis. A review found that the 'n_live' number (number of actively used points used in the nested sampling process [25]) used in the Nautilus nested sampling algorithm was too small. Increasing n_live=50 to n_live=300 increased the number of the live points. Thus, the resolution and accuracy of the evidence estimation was increased and led to the expected results. n_live=300 was used throughout to reduce systematic errors.

From table 1 we can see that the 'bar_0' and 'bar_1' results for the $\mathcal{L}_{max}$ R_e are within a 5% tolerance interval of the expected results. The small and symmetric uncertainties indicate a Gaussian-like error distribution (figure 4) and clean posterior behaviour being tightly constrained and a statistically robust fit. We can conclude that the light profile fitting analysis is accurate.

Simulated Image	Fitting model	$R_e^{\mathcal{L}max}$ (arcsec)	R_E, (arcsec)	$\lvert R_E - R_e \rvert$, (arcsec)	$\lvert R_E - R_e \rvert$ (%)
'bar_0'	Double Sérsic	$0.306^{+0.0031}_{-0.0030}$	0.300	0.006	2.000
'bar_1'	Double Sérsic	$0.786^{+0.0046}_{-0.0048}$	0.800	0.014	1.750

Table 1: Effective radii maximum log likelihood ($R_e^{\mathcal{L}max}$) results for 'bar_0' and 'bar_1' compared to expected effective radii (R_E) results.

As we are dealing with different datasets and there is no standard scale for $\mathcal{L}$ to compare fits, it was more meaningful to compare $\mathcal{L}$'s.

$$\Delta\mathcal{L} = \mathcal{L}_{barred} - \mathcal{L}_{unbarred} \tag{2.2.3}$$

With larger $\Delta\mathcal{L}$ indicating that the barred (double Sérsic) model produced a better fit.

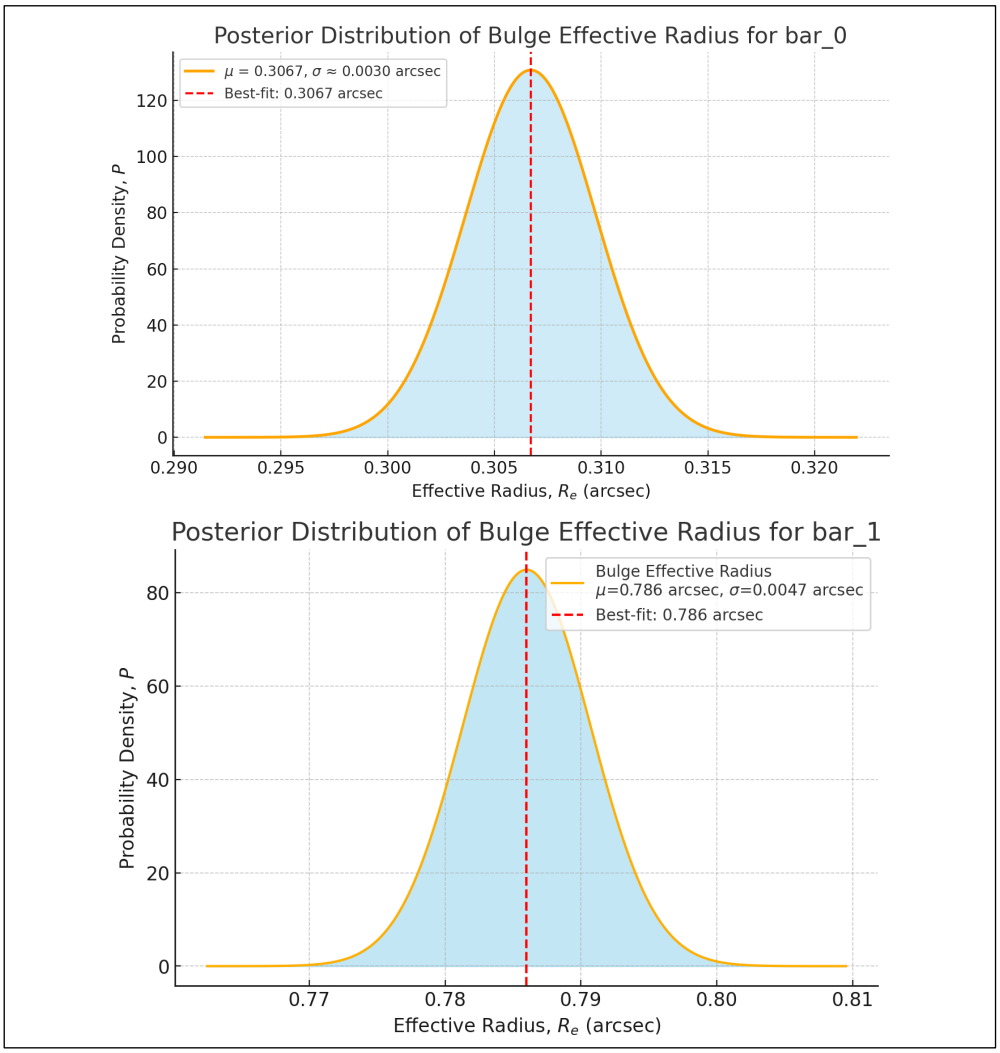

Figure 4: Posterior distribution of the bulge R_e for bar_0 and bar_1. The narrow and symmetric probability density function, illustrates the tight constraint on the fitted effective radius.

2.3 Quantitative assessment of the presence of a bar

It's not known whether real datasets contain a bar. To solve this issue, model comparison was chosen. Model comparison enables the quantitative determination of a bar by fitting the barred and unbarred model to data and comparing the quality of the fits by comparing the $\mathcal{L}_{max}$ value. To test this method was accurate, a single Sérsic model was fitted to 'bar_0' and 'bar_1' datasets. This was to verify that the single Sérsic fits are worse than the double Sérsic model fits that were done previously.

However, extra Sérsic components might improve any fit, barred or not, due to the extra parameters that increase representational capacity and therefore capturing more complex patterns in the data [26].

To rule this out a galaxy simulated to have no bar ('no_bar') was loaded into the program and fitted with the single Sérsic model, then with the double Sérsic model. This verified that the $\mathcal{L}$ values do not improve when a secondary Sérsic profile representing a bar was included in the

fitting. It could now be said that there is indeed a quantitative method of determining the presence of a bar in a galaxy.

Simulated image	Fitting model	$\mathcal{L}_{max}$
bar_0	Single Sérsic	63850.19510824
bar_0	Double Sérsic	67770.01731120
$\Delta\mathcal{L}_{max}$		3919.822203
$\Delta\mathcal{L}_{max}$ (%)		6.139%
Simulated image	**Fitting model**	$\mathcal{L}_{max}$
bar_1	Single Sérsic	66648.40954331
bar_1	Double Sérsic	70832.05814655
$\Delta\mathcal{L}_{max}$		4183.648603
$\Delta\mathcal{L}_{max}$ (%)		6.277%
Simulated image	**Fitting model**	$\mathcal{L}_{max}$
no_bar	Single Sérsic	67499.18813772
no_bar	Double Sérsic	67516.10257981
$\Delta\mathcal{L}_{max}$		16.91444209
$\Delta\mathcal{L}_{max}$ (%)		0.025%

Table 2: Maximum log likelihood ($\mathcal{L}_{\max}$) results from single and double Sérsic model fits on simulated galaxies.

Table 2 shows a significant increase in $\mathcal{L}_{max}$ value for both 'bar_0' and 'bar_1' when a double Sérsic model is used, with a $\Delta\mathcal{L}_{max}\sim 4000$. Confirming the barred model produces a better fit when fitting a barred galaxy image.
When looking at $\Delta\mathcal{L}_{max}$ for 'no_bar' there is small increase of ~ 16.9 when a double Sérsic is used. An increase of 0.025%. Compared to an increase of 6.139% and 6.277% for 'bar_0' and 'bar_1' respectively, the 'no_bar' increase is significantly smaller and inspection of the normalised residual maps shows minimal improvement and therefore can be dismissed as negligible. Thus, it can be concluded that a double Sérsic model does not produces a better fit when applied to a bar-less galaxy image. Confirming the effectiveness of the quantitative method.

The results from table 2 provided boundaries for the JWST image analysis:

- $\Delta\mathcal{L}_{max} > 5\%$: strong bar indicator, since both 'bar_0' and 'bar_1' exceed that.
- $\Delta\mathcal{L}_{max} > 1\%$: bar indicator as it comfortably separates the 'bar_0'/'bar_1' cases from the 'no_bar' case. Allows for large residuals expected with real galaxies. Visual inspection required.
- $\Delta\mathcal{L}_{max} < 1\%$: no bar indicator. These values are low and suggest the second Sérsic component doesn't add meaningful explanatory power.

2.4 JWST image analysis

Inspection of all model results were done to ensure that none of the parameter results were at the bounds of the priors. A parameter result at a prior bound would indicate that the non-linear search would have continued if not for the bound, resulting in an inaccurate model result [27]. Parameters at prior bounds had their limits increased by 0.5, then rechecked to

ensure they no longer sat at a bound. The only parameter result allowed to fall on a prior boundary was the Sérsic index of the double Sérsic model bar component as it was forced.

Quantitatively inferring the presence of a bar in a real galaxy is highly challenging. Visually there could be confidence that there is a bar but model comparison results do not support this or vice versa. That's why quantitative model comparison analysis was paired with a visual inspection.

3 Results and Discussion

For this study the galaxies were unknown and referenced by 'dataset_X' to keep the presence of a bar unknown by not knowing the galaxy. Knowing the bar-presence result would introduce unwanted bias during visual inspection. 3 visually distinct galaxies (figure 5) were selected by visual inspection to test the method across varied morphologies. Light profiles cover a wide range of values so were visualised on a log10 scale to enhance faint outer structure (figure 6).

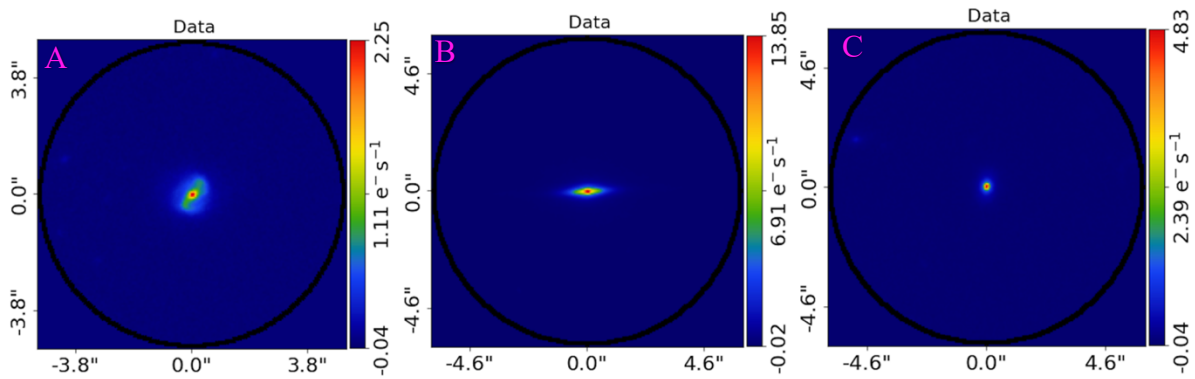

Figure 5: JWST image data: (A) dataset_3, (B) dataset_4, (C) dataset_6. Masking radius shown by the black circle.

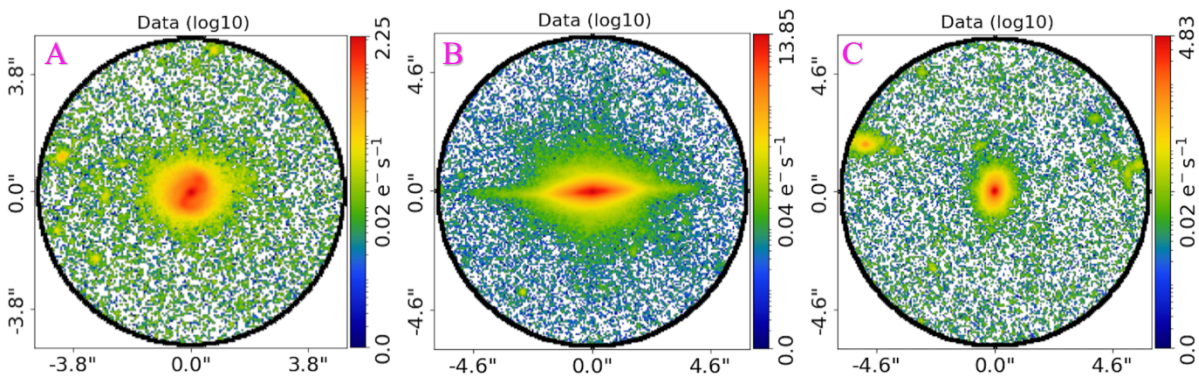

Figure 6: JWST image data on a log10 scale: (A) dataset_3, (B) dataset_4, (C) dataset_6. Masking radius shown by the black circle.

3.1 Results

All 3 galaxy fits resulted in the double Sérsic having a higher $\mathcal{L}$ value (table 3), which was expected, with dataset_4 having the largest increase with $\Delta\mathcal{L}_{max} = 6.6682\%$, dataset_6 having the smallest with $\Delta\mathcal{L}_{max} = 0.3837\%$ and dataset_3 with $\Delta\mathcal{L}_{max} = 3.1222\%$. This was unsurprising as visual inspection of the dataset_4 image (figure 5B and 6B) revealed a very flat emission. The $\Delta\mathcal{L}_{max}$~6% was also consistent with the method testing on simulated galaxies (table 2), so it could be said with high certainty that dataset_4 contains a bar. Visual inspection confirmed this and found resemblance to the simulated barred galaxies.

Dataset_3's $\Delta\mathcal{L}_{max}$ was 0.5x that of the method testing results on the simulated galaxies ($\Delta\mathcal{L}_{max}$~6%) but still much higher than the 'no_bar' results ($\Delta\mathcal{L}_{max} = 0.025\%$). Suggesting that dataset_3 didn't resemble the simulated galaxies as much as dataset_4. However, still a strong $\Delta\mathcal{L}_{max}$ increase, with $\Delta\mathcal{L}_{max} > 1\%$. Visual inspection confirmed the model comparison and concluded that dataset_3 most likely contains a bar.

Method		**Galaxy**		
		dataset_3	dataset_4	dataset_6
Model Comparison	$\mathcal{L}_{max}$, (single Sérsic)	55806.17401028	79448.08184727	87067.04195232
	$\mathcal{L}_{max}$, (double Sérsic)	57548.57417307	84745.85394052	87401.09374824
	$\Delta\mathcal{L}_{max}$	1742.400163	5297.772093	334.0517959
	$\Delta\mathcal{L}_{max}$%	3.1222%	6.6682%	0.3837%
	Conclusion	Barred	Barred	Unbarred
Visual Inspection	Visual confidence of a bar	Y	Y	N
Overall conclusion		Barred	Barred	Unbarred

Table 3: Model comparison results, visual inspection results and overall conclusion of the presence of a bar.

Dataset_6's $\Delta\mathcal{L}_{max} = 0.3837\%$. Far lower than the previous $\Delta\mathcal{L}_{max}$ and much closer to the 'no_bar' $\Delta\mathcal{L}_{max}$ of 0.025%. $\Delta\mathcal{L}_{max} < 1\%$ indicating no bar. Visual inspection resulted in no bar also. Comparing the normalised residual map's (figure 7 and 8), the double Sérsic displayed a clear unnatural straight line with intensity ~ -1 cutting through the map. Since the only difference between the models is the additional bar component in the double Sérsic model, it can be concluded that this is due to the non-linear search algorithm attempting to fit the bar. This isn't present in the single Sérsic normalised residual map and when comparing to the double Sérsic normalised residuals, the single Sérsic has produced a better fit. Large residuals were present amongst all results, especially towards the centre of the images which were expected due to the inherently complex nature of real galaxies being fitted with fairly simplistic models. To improve this a more sophisticated model could be used for fitting to better capture the different aspects of the galaxies.

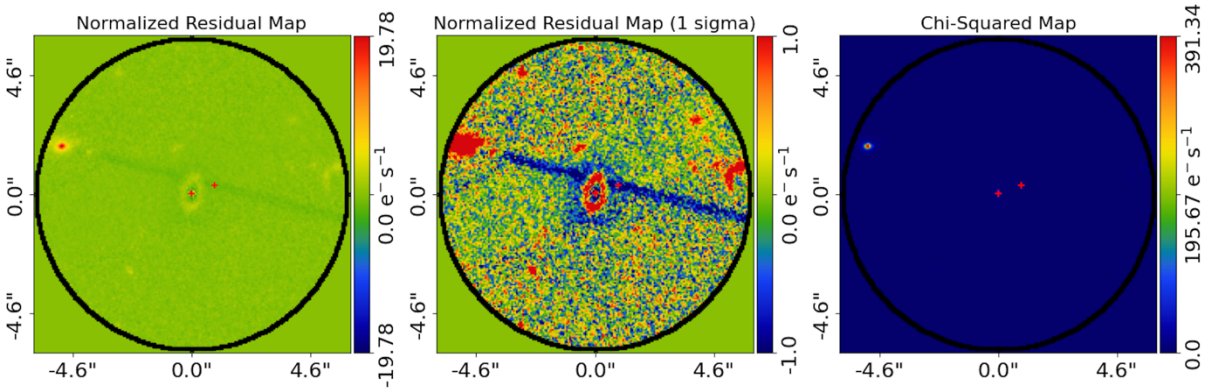

Figure 7: Dataset_6 double Sérsic model fit maps of normalised residuals, normalised residuals (1 sigma) and chi-squared.

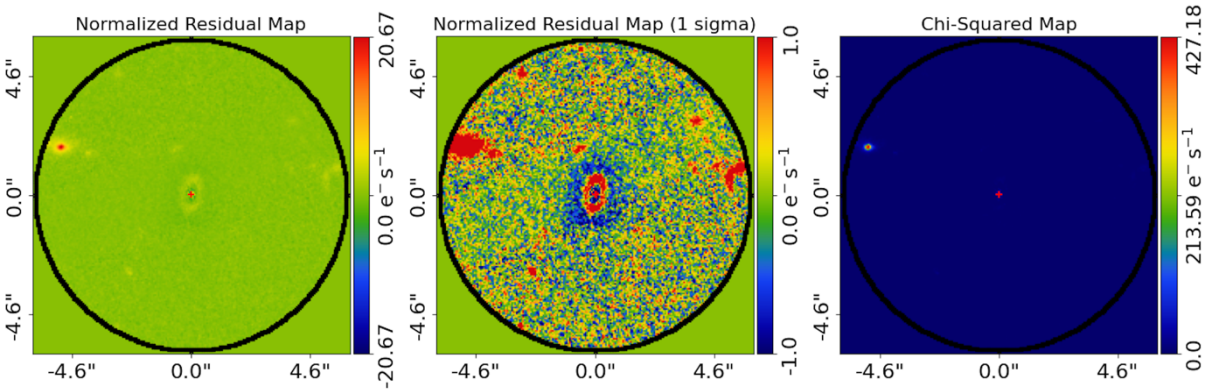

Figure 8: Dataset_6 single Sérsic model fit maps of normalised residuals, normalised residuals (1 sigma) and chi-squared.

3.2 Uncertainty analysis

Dataset	**Model**	$\mathcal{L}_{max}$	$\langle\mathcal{L}\rangle$	σ
dataset_3	Double Sérsic	57548.57417307360	57539.62670020920	7.572251238588040
	Single Sérsic	55806.17401027770	55800.31542855290	6.353423228743420
dataset_4	Double Sérsic	84745.85394051610	84735.86918591090	8.050060802476000
	Single Sérsic	79448.0818472683	79442.71258721030	6.020631834802830
dataset_6	Double Sérsic	87401.09374823630	87393.30090005640	7.167578747066570
	Single Sérsic	87067.04195231930	87057.38754062770	6.60602190520219

Table 4: Summary of maximum log likelihoods ($\mathcal{L}_{max}$), mean log likelihoods ($\langle\mathcal{L}\rangle$)and standard deviations (σ), for single and double Sérsic models across JWST datasets.

The σ, of the $\mathcal{L}_{max}$ values provide an estimate of the uncertainty associated with the model fits. As seen in table 4, the σ is consistently small (6.0-8.1) across all models. The tight spread indicates the fits are well constrained, thus little stochastic variation among near-optimal solutions. Although, uncertainties in the $\mathcal{L}_{max}$ values were not explicitly calculated, the narrow posterior distributions of the fitted parameters suggest that stochastic variations in $\mathcal{L}_{max}$, are minimal. Thus, $\Delta\mathcal{L}$ values are statistically robust and not noise-driven.

3.3 SFR reduction and stellar nurseries

This study presents evidence supporting the dual role of bars in galaxy evolution — as agents of star formation quenching and as stellar nurseries. In dataset_3, intensity profiles reveal a distinct drop in intensity within the co-rotation radius (figure 9), consistent with bar-induced quenching, as described by George et al. [9], Newnham et al. [10] and Scaloni et al. [11]. The depleted intensity suggests reduced specific star formation due to bars funnelling gas inward and depleting the surrounding disk of star-forming material.

In contrast, datasets_3 and _4 show elevated relative intensity along the whole bar length, peaking at the centre. This enhanced intensity supports the theory that bars also act as stellar nurseries, concentrating inflowing gas and triggering central star formation (Vera et al. [2], Renaud et al. [13], Lin et al. [14]). These spatial patterns of intensity — depressed in the inner disk, enhanced along the bar — closely match contemporary simulations [4] and large survey trends.

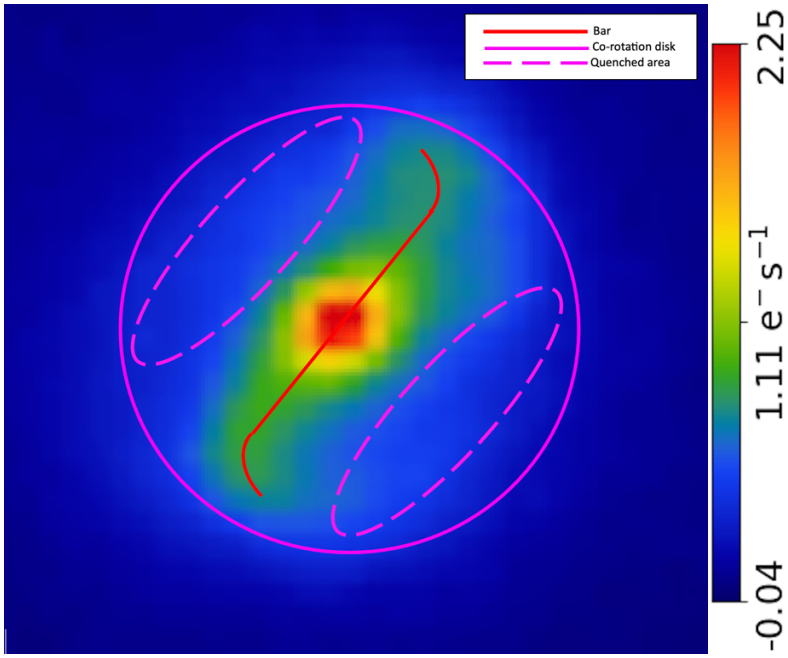

Figure 9: Schematic of magnified dataset_3, showing the bar, co-rotation disk and quenched areas.

Critically, these findings are grounded in statistically robust bar detections using $\Delta\mathcal{L}$ thresholds. Dataset_4's $\Delta\mathcal{L}$=6.6682% and dataset_3's $\Delta\mathcal{L}$=3.1222% confidently confirm bar presence, reinforcing the validity of the physical interpretations drawn from intensity structure. The quantitative bar identification scheme developed in this study could be systematically applied to existing JWST deep fields to construct statistically robust barred galaxy fractions as a function of redshift and morphology.

While this study does not include direct star formation rate tracers, the intensity-based analysis offers a repeatable framework that links bar presence to plausible evolutionary effects. This lays the groundwork for extending the method to larger samples and integrating multiwavelength data to assess bar-driven evolution more comprehensively.

4 Conclusion

To conclude, this project developed and validated a quantitative method for identifying bars in galaxies using Sérsic light profile fitting and log-likelihood model comparison. By introducing a secondary low-index (n=0.5) Sérsic component to model bars, and establishing $\Delta\mathcal{L}$ thresholds, this method provided a statistically robust and reproducible approach for determining bar presence. Validation against simulated galaxies demonstrated that the barred models consistently yielded $\Delta\mathcal{L}$ increases of ~6%, while unbarred systems showed negligible improvements, confirming the method's reliability. Application to JWST imaging data further reinforced its effectiveness. In three visually diverse galaxies, the method produced consistent results with visual inspection, demonstrating its robustness across varying morphologies. This hybrid approach - combining quantitative fitting with visual validation - ensures both statistical rigour and interpretative reliability.

Beyond bar detection, the analysis of light distributions revealed structural signatures aligned with current theories of bar-driven galaxy evolution. Intensity profiles revealed signs of bar-induced quenching within co-rotation radii, as well as enhanced stellar activity along the bar. While intensity was used as a proxy, these findings align closely with contemporary literature and simulations, supporting bars' role in redistributing star-forming material. In summary, this project contributes a generalisable method for bar detection and offers observational support for key evolutionary roles of bars. Applying this method to larger datasets with spectral data could deepen understanding of bar-driven evolution across cosmic time.

References

[1] G. Paturel *et al.*, (2003), 'HYPERLEDA', *A&A*, **412**, 1, p.45.

[2] M. Vera, S. Alonso, and G. Coldwell, (2016), 'Effect of bars on the galaxy properties', *A&A*, **595**, A63.

[3] D. A. Gadotti, (2009), 'Barred galaxies: An observer's perspective', presented at Chaos in Astronomy.

[4] E. Athanassoula, (2011), 'Bars and secular evolution in disk galaxies: Theoretical input', in *Secular Evolution of Galaxies*, Cambridge, Cambridge University Press.

[5] K. Sheth *et al.*, (2008), 'Evolution of the Bar Fraction in COSMOS: Quantifying the Assembly of the Hubble Sequence', *ApJ*, **675**, 2, p.1141.

[6] K. Kuijken and M. R. Merrifield, (1995), 'Establishing the connection between peanut-shaped bulges and galactic bars', *ApJ*, **443**, L13.

[7] NASA, (2025), 'https://science.nasa.gov/asset/hubble/barred-spiral-galaxy-ngc-1300/'.

[8] James. W. Nightingale *et al.*, (2023), 'PyAutoGalaxy: Open-Source Multiwavelength Galaxy Structure & Morphology', *JOSS*, **8**, 81.

[9] K. George, S. Subramanian, and K. T. Paul, (2019), 'Significance of bar quenching in the global quenching of star formation', *A&A*, **628**, A24.

[10] L. Newnham *et al.*, (2020), 'The H I morphology and stellar properties of strongly barred galaxies: Support for bar quenching in massive spirals', *MNRAS*, **492**, 4, p.4697.

[11] L. Scaloni *et al.*, (2024), 'The impact of stellar bars on star-formation quenching: Insights from a spatially resolved analysis in the local Universe', *A&A*, **687**, A255.

[12] V. Cuomo, Y. Hee Lee, C. Buttitta, J. A. L. Aguerri, E. Maria Corsini, and L. Morelli, (2021), 'Bar pattern speeds in CALIFA galaxies', *A&A*, **649**, A30.

[13] F. Renaud *et al.*, (2015), 'Environmental regulation of cloud and star formation in galactic bars', *MNRAS*, **454**, 3, p.3299.

[14] L. Lin *et al.*, (2020), 'SDSS-IV MaNGA: The indispensable role of bars in enhancing the central star formation of low-z galaxies', *MNRAS*, **499**, 1, p.1406.

[15] J. Nightingale, (2025), 'https://github.com/Jammy2211/BSc_Galaxies_Project/blob/master/tutorial.ipynb'.

[16] P. Prugniel and F. Simien, (1997), 'The fundamental plane of early-type galaxies: Non-homology of the spatial structure', *A&A*, **321**, 1, p.111.

[17] J. Sérsic, (1968), '*Atlas de Galaxias Australes'*. Observatorio Astronomico, Universidad Nacional de Cordoba.

[18] I. D. Gargiulo *et al.*, (2022), 'High and low Sérsic index bulges in Milky Way- and M31-like galaxies: origin and connection to the bar with TNG50', *MNRAS*, **512**, 2, p.2537.

[19] G. de Vaucouleurs, (1948), 'Recherches sur les Nebuleuses Extragalactiques', *Ann. Astrophys*, **11**, p.247.

[20] A. W. Graham and S. P. Driver, (2005), 'A Concise Reference to (Projected) Sérsic $R^{1/n}$ Quantities, Including Concentration, Profile Slopes, Petrosian Indices, and Kron Magnitudes', *PASA*, **22**, 2, p.118.

[21] T. Weinzirl, S. Jogee, S. Khochfar, A. Burkert, and J. Kormendy, (2009), 'Bulge n and B/T in high-mass galaxies: Constraints on the origin of bulges in hierarchical models', *ApJ*, **696**, 1, p.411.

[22] I. Trujillo, J. A. L. Aguerri, J. Cepa, and C. M. Gutiérrez, (2001), 'The effects of seeing on Sérsic profiles - II. The Moffat PSF', *MNRAS*, **328**, 3, p.977.

[23] (2025), 'JWST Pocket Guide', STScI.

[24] M. Hadi, G. McKay, M. R. Samarghandi, A. Maleki, and M. S. Aminabad, (2012), 'Prediction of optimum adsorption isotherm: Comparison of chi-square and Log-likelihood statistics', *Desalination Water Treat*, **49**, 1–3, p.81.

[25] J. U. Lange, (2023), 'nautilus: boosting Bayesian importance nested sampling with deep learning', *MNRAS*, **525**, 2, p.3181.

[26] C. Y. Peng, L. C. Ho, C. D. Impey, and H.-W. Rix, (2002), 'Detailed Structural Decomposition of Galaxy Images', *AJ*, **124**, 1, p.266.

[27] L. A. Gibson and K. B. McAuley, (2025), 'Bayesian parameter estimation using truncated normal distributions as priors for parameters in fundamental models of chemical processes', *CJCE*, **103**, 2, p.649.